Editors' Suggestion Featured in Physics

Magnetic skyrmion lattice disclinations in pentagon- and heptagon-shaped FeGe nanostructures

Thibaud Denneulin,[1,*] Nikolai S. Kiselev,[2] Vladyslav M. Kuchkin,[3] and Rafal E. Dunin-Borkowski[1]
[1]Ernst Ruska-Centre for Microscopy and Spectroscopy with Electrons, Forschungszentrum Jülich, 52425 Jülich, Germany
[2]Peter Grünberg Institute and Institute for Advanced Simulation, Forschungszentrum Jülich and JARA, 52425 Jülich, Germany
[3]Department of Physics and Materials Science, University of Luxembourg, L-1511 Luxembourg

(Received 11 January 2026; revised 29 April 2026; accepted 12 May 2026; published 7 July 2026)

Magnetic skyrmions in chiral magnets typically arrange into hexagonal lattices, with their structural order influenced by factors such as temperature, external magnetic fields, and geometric constraints. While translational defects in skyrmion lattices such as dislocations have been extensively studied, individual angular defects, or *disclinations*, remain largely unexplored. Here, we report on the stabilization of fivefold and sevenfold disclinations in pentagon- and heptagon-shaped FeGe single-crystal nanostructures created using focused ion beam milling. The magnetic and elastic structures of the disclinated lattices are investigated using Fresnel imaging and off-axis electron holography in a transmission electron microscope. The results are supported by micromagnetic simulations and analytical models based on linear elasticity theory.

DOI: 10.1103/nwd2-1hk9

I. INTRODUCTION

Fivefold symmetry is common in biological systems, for instance, in flowers, starfishes, viruses [1], and protein supermolecules [2]. In contrast, it is much less common in crystals as it is geometrically impossible to create a periodic fivefold lattice. There are a few historical reports of *fiveling* in mineralogy, in macrometer-scale crystals of gold and copper [3,4]. In a fiveling (or pentatwin), five wedge-shaped single crystals separated by twin boundaries are distributed around a common axis and produce a pentagonal shape. In the 1960s, different studies have reported that synthesized metallic nanoparticles can exhibit pentatwins based on transmission electron microscopy (TEM) observations [5–7]. A pentatwin can also be described as a *disclination*, a type of crystalline defect in which rotational symmetry is violated [8,9]. The term derives from *disinclination*, which was first introduced in the field of liquid crystals [10]. There are also certain structural relations between pentatwins and quasicrystals discovered later in the 1980s [11]. Due to the missing wedge, a disclinated crystal experiences an elastic deformation which varies circularly around the quintuple junction [12,13]. In two-dimensional hexagonal systems, fivefold and sevenfold disclinations can also be created by the removal or the addition of a 60° wedge [14]. Two-dimensional (2D) disclinations have been described, for instance, in bubble raft crystals on water [15], in topological crystalline insulators [16] and in graphene [17]. In a graphene nanotube, a fivefold disclination can be observed at the apex, facilitating the closure of the nanotube [18]. More generally, disclinations are a key ingredient of curved geometries [19].

Magnetic skyrmions are swirling spin textures possessing properties of classical particles with potential applications in the field of spintronics [20]. They were first observed at low temperature in noncentrosymmetric B20 compounds, such as MnSi and FeGe [21,22], where they are stabilized by the balance between the exchange interaction and the Dzyaloshinskii-Moriya interaction [23,24]. Skyrmions in chiral magnets can form two-dimensional hexagonal lattices in particular conditions of temperature and magnetic fields [21,22,25]. Similar to atomic lattices, skyrmion lattices can exhibit crystalline defects such as dislocations and grain boundaries depending on the geometric constraints [26–28]. These defects also play a role in the magnetic phase transitions that occur when increasing the external magnetic field or the temperature [29–33]. This *melting* phenomenon and the associated disordering are described by the Kosterlitz, Thouless, Halperin, Nelson, and Young theory (KTHNY theory) [34–36]. In the presence of large external magnetic fields, 5–7 dislocations (i.e., pairs of 5-membered and 7-membered skyrmion rings) dissociate into individual disclinations during the transition between the *solid* and *liquid* phases, also called the *hexatic* phase [30]. Disclinations in chiral magnets have previously been observed in one-dimensional lattices of the *helical* ground state, which form without the need for external magnetic fields [37,38]. However, disclinations in the hexatic phase are particularly difficult to observe due to the high mobility of the skyrmions in the presence of large external magnetic fields. In this study, we report on the stabilization of fivefold and sevenfold disclinations in the skyrmion *solid* phase of FeGe in pentagon- and heptagon-shaped single-crystal nanostructures observed using Lorentz TEM. As structural defects, disclinations are important for the understanding of the physical properties of skyrmion lattices and may play a role in prospective applications in spintronic devices.

*Contact author: t.denneulin@fz-juelich.de

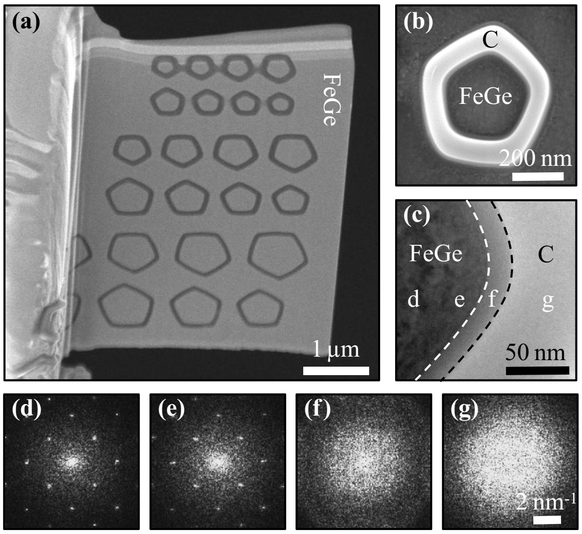

FIG. 1. Sample description. (a) Representative scanning electron microscopy image of a TEM lamella of FeGe patterned with pentagons of different sizes. (b) TEM image of a small pentagon. (c) Magnified image of the FeGe/C interface. (d)–(g) Fourier transforms of different regions indicated in (c).

II. RESULTS

A. Sample description

Figure 1(a) shows a TEM lamella of FeGe containing pentagon-shaped patterns of different sizes produced by focused ion-beam (FIB) milling following the method described in the Supplemental Material 1 [39]. Carbon contours that are approximately 100 nm thick around the pentagons were created using ion-beam-induced deposition. The edges of the pentagons were intentionally made slightly rounded (convex), which may help accommodate the disclination strain associated with the angular deficit. Figures 1(b) and 1(c) show magnified images of a small pentagon and the FeGe/C interface. The interface shows a FIB-damaged layer of 20 ± 5 nm thick, as indicated by dashed lines. The Fourier transforms shown in Figs. 1(d)–1(g), calculated in different regions of the image, show that the inner part of the pentagon is monocrystalline [Figs. 1(d) and 1(e)], whereas the damaged layer and the carbon layer are amorphous [Figs. 1(f) and 1(g)].

Figure 2(a) shows an image of a pentagon with a side length of $l = 320$ nm and a radius of $r = l/[2\sin(36^\circ)] = 272$ nm, which was investigated using Lorentz TEM at a temperature of 220 K. As shown schematically in Fig. 2(b), the fivefold disclination state is obtained for a total number of skyrmions,

$$S = 1 + \sum_{n=1}^{N} 5n, \tag{1}$$

where n is the skyrmion ring number and N is the total number of rings that the pentagon can contain. It can be expected that $N \approx (r/d - 1)$, where d is the interskyrmion distance, although this relation is approximate because the effective magnetic area may be reduced by the FIB-damaged layer. A value of $d = 88$ nm was previously measured in similar conditions of temperature and magnetic fields [40]. Therefore, for the pentagon size considered here, the maximum number of skyrmion rings is expected to be $N = 2$ and so the total number of skyrmions in the disclination state should be $S = 16$.

B. Magnetic field evolution and skyrmion crystals

Figure 2(c) is a series of Fresnel images that shows the evolution of the magnetic domain structure in the presence of external magnetic fields from the helical ground state at 0 mT to the skyrmion lattice phase at 210 mT (a more detailed field series is shown in the Supplemental Material 2 [39]). During the first field increase, the number of skyrmions is often not large enough to fill the entire pentagon. Here, only 13 skyrmions are obtained at 210 mT. By partially reducing the magnetic field to 110 mT, additional stripe domains and skyrmions often spontaneously nucleate. Consequently, after

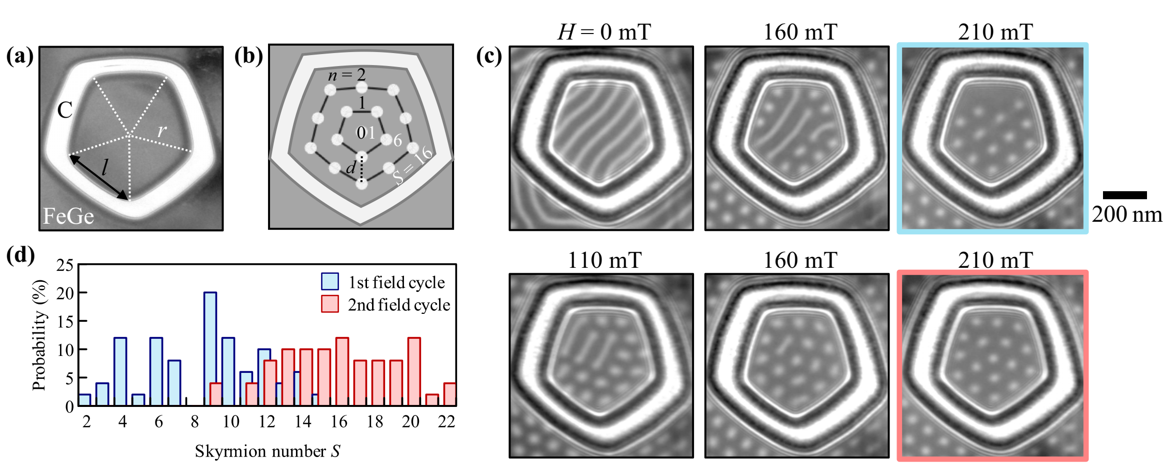

FIG. 2. LTEM of a pentagon-shaped sample with applied magnetic fields. (a) In-focus TEM image of a pentagon-shaped sample with a side length $l = 320$ nm. (b) Schematic showing a fivefold disclination with 16 skyrmions. (c) Fresnel images with a 500 μm defocus obtained at 220 K at the external magnetic fields indicated in the figure. (d) Plot showing the probability to obtain a given skyrmion number S after the first and second field cycles.

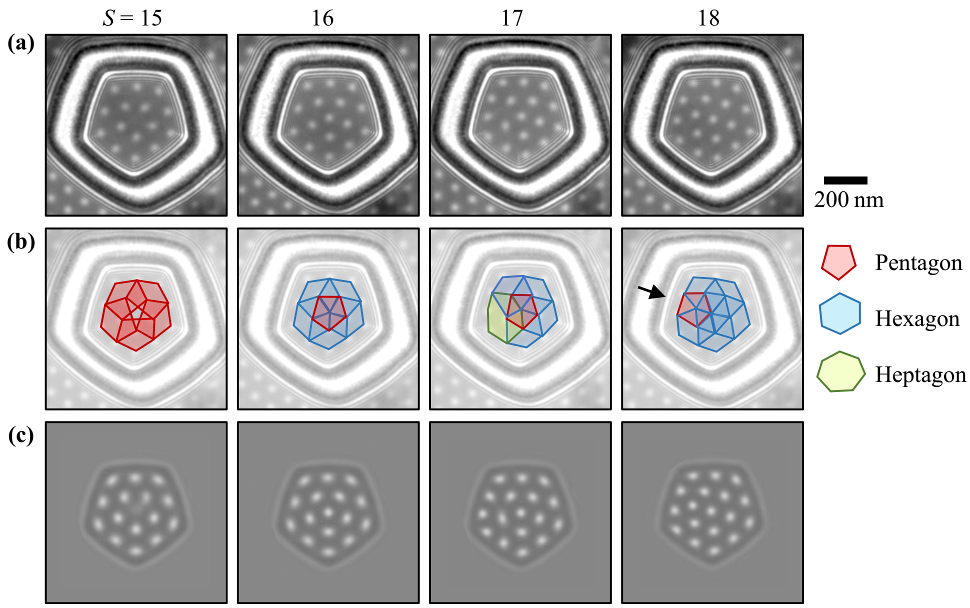

FIG. 3. LTEM of skyrmion lattices in a pentagon-shaped sample. (a) Fresnel images with a 500 µm defocus obtained at 220 K and with an external magnetic field of 230 mT. The images contain lattices with different skyrmion numbers indicated in the figure. (b) Previous images overlaid with pentagons, hexagons, and heptagons. (c) Corresponding Fresnel images calculated from micromagnetic simulations.

a second increase of the field, a larger number of skyrmions is obtained and the lattice can occupy the entire pentagon geometry. Here, the last image obtained at 210 mT shows 17 skyrmions, but the number of skyrmions can vary for each new field cycle. Figure 2(d) shows the probability to obtain a given skyrmion number S, which was measured by cycling the field 50 times, between 0 and 210 mT in blue and then between 110 and 210 mT in red. The number of skyrmions ranges from 2 to 15 during the first cycle and from 9 to 22 during the second one. It shows that performing multiple cycles helps to generate additional domains and skyrmions. Nevertheless, the distribution remains broad, indicating that the skyrmion number is highly probabilistic. At 220 K, thermal energy is likely to drive the system toward a different metastable configuration after each field cycle. Here, the disclination state with 16 skyrmions could not be obtained during the first cycle, but the probability of obtaining it during the second cycle was 12%.

Figure 3(a) shows Fresnel images of lattices with different skyrmion numbers ($S = 15$ to 18) obtained by cycling the field. In Fig. 3(b), the lattice was segmented into pentagons, hexagons, and heptagons to indicate the number of nearest neighbors. As expected, in the fivefold disclination state with $S = 16$, the central skyrmion at $n = 0$ has five neighbors, whereas the skyrmions of the inner ring $n = 1$ have six neighbors. Interestingly, when $S = 15$, the lattice still shows a fivefold symmetry, but the central skyrmion at $n = 0$ is absent. Fresnel images calculated from micromagnetic simulations in Fig. 3(c) confirm these observations. When $S = 17$, the additional skyrmion with respect to $S = 16$ is placed on the outer ring $n = 2$, which breaks the fivefold symmetry. A 5–7 dislocation appears with the pentagon located in the middle and the heptagon in one of the five corners. When $S = 18$, another skyrmion is added to the inner ring, $n = 1$, forming a hexagon in the middle and a pentagon on one side. For $S = 17$ and 18, the additional skyrmions are located on the left side of the pentagon. This is likely due to a slight geometric irregularity: the top-left edge [indicated by an arrow in Fig. 3(b)] is slightly longer (∼340 nm) than the others (∼320 nm), which could favor the accommodation of additional skyrmions on that side. A similar study carried out on a heptagon-shaped sample is shown in the Supplemental Material 3 [39].

C. Magnetic and structural analysis of a fivefold disclination

To perform a more advanced analysis of the disclination, an in-focus off-axis electron hologram of the pentagon-shaped sample was recorded in Fig. 4(a). Figures 4(b)–4(e) show the reconstructed magnetic phase image ϕ_{mag}, the magnitude and direction of the in-plane magnetic induction field $\boldsymbol{B}_{\perp}$, and average profiles extracted from the phase image along radial and tangential directions. It can be observed in Fig. 4(c) that the central skyrmion has a pentagon shape and is slightly smaller than the other skyrmions. As expected, the magnetic field in Fig. 4(d) of the skyrmions rotates around their core, which indicates a Bloch-type texture. The profiles in Fig. 4(e) show that the interskyrmion distance d_r and skyrmion diameter ϕ_r along the radial direction (solid red profile) are shorter than the corresponding distances d_t and ϕ_t along the tangential direction (dashed blue profile). In a fivefold disclination, the removal of a $2\pi/6$ wedge induces an elongation of the five remaining wedges along the circular direction. A similar analysis of a sevenfold disclination is presented in the Supplemental Material 4 [39], where, conversely, $d_r > d_t$ due to the addition of a wedge and the resulting compression along the circular direction.

Figures 4(f)–4(j) show corresponding micromagnetic simulations of a fivefold disclination. The simulated images confirm that the central skyrmion is slightly smaller than the surrounding skyrmions, and the five wedges are elongated

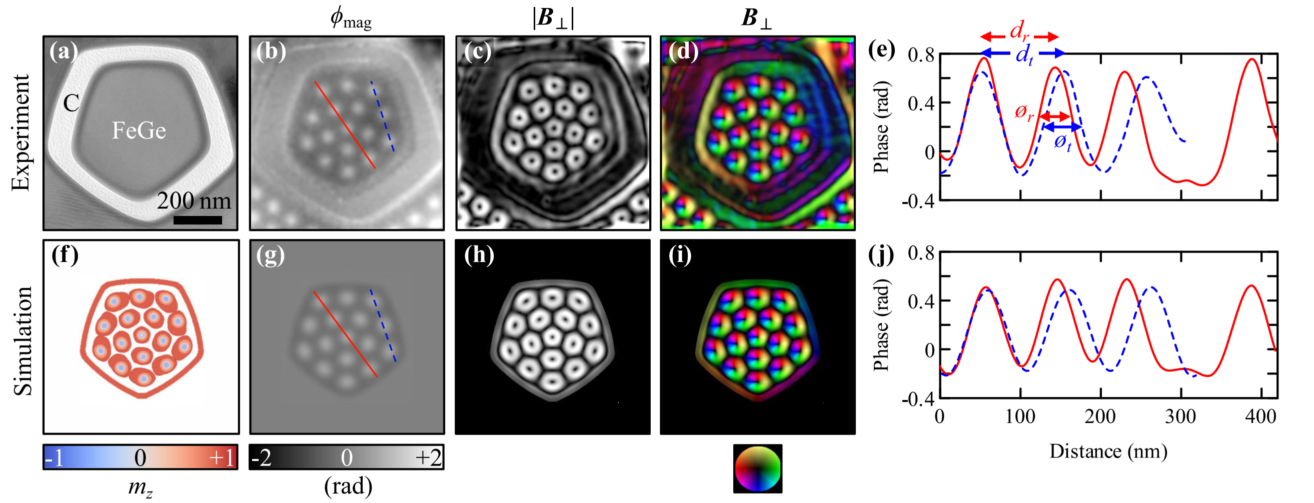

FIG. 4. Electron holography of a fivefold disclination. (a) Electron hologram of a pentagon-shaped sample recorded with an external magnetic field of 240 mT. (b) Magnetic phase image ϕ_{mag} obtained using off-axis electron holography after subtraction of a phase image recorded at room temperature. (c) Magnitude of the in-plane magnetic induction field $|\boldsymbol{B}_\perp|$. (d) Corresponding color-coded map showing the direction of $\boldsymbol{B}_\perp$. (e) Phase profiles extracted from (b) along the solid and dashed lines. (f) Isosurface representation of the normalized out-plane component m_z of a magnetization model calculated using micromagnetic simulation. (g)–(j) Corresponding phase image, magnetic field maps, and phase profiles.

along the circular direction around the core. It can be noticed in Fig. 4(f) that this elongation is associated with a twist of the skyrmions along the electron beam direction, which was previously discussed in the context of skyrmion braids [41]. Table I compares the mean interskyrmion distances $(\overline{d_r}, \overline{d_t})$ and skyrmion diameters $(\overline{\phi_r}, \overline{\phi_t})$ of the experimental and simulated disclinations. Experimental and simulated values of $(\overline{d_r}, \overline{d_t})$ are relatively close, but the experimental values of $(\overline{\phi_r}, \overline{\phi_t})$ are slightly lower than the simulated ones. It is shown in the Supplemental Material 5 [39] that skyrmion diameters are dependent on the applied magnetic field, in particular along the tangential direction. At low magnetic fields, the skyrmions stretch along the tangential direction to fill space. On the other hand, the interskyrmion distances were found to be nearly constant as a function of the applied field.

To investigate the structure of the disclination in more detail, we identified the center-of-mass coordinates of the 16 skyrmions in the phase image, as shown in Fig. 5(a). The local orientational order parameter Ψ_6 of the five hexagons was calculated as

$$\Psi_6(r_j) = \frac{1}{6}\sum_{k=1}^{6} \exp(i6\theta_{jk}), \qquad (2)$$

TABLE I. Skyrmion distances and diameters. Mean interskyrmion distances $\overline{d}$ and skyrmion diameters $\overline{\phi}$ along the tangential t and radial r directions of the experimental and simulated disclinations. Ratios of experimental and simulated values are also reported.

	$\overline{d_r}$	$\overline{d_t}$	$\overline{\phi_r}$	$\overline{\phi_t}$
Experiment (nm, ±2 nm)	88	103	41	46
Simulation (nm)	88	108	44	55
Ratio Expt. / Sim.	1.00	0.95	0.93	0.83

with r_j the position of a skyrmion, and θ_{jk} the angle between the line connecting the central skyrmion j and its neighbors k relative to an arbitrary axis [42]. The parameter $\theta = \arg(\Psi_6)/6$ shown in Fig. 5(b) represents the local orientation of the hexagons. The modulus $|\Psi_6|$ shown in Fig. 5(c) represents the degree of *hexagonality* with $|\Psi_6| = 1$ for a perfect hexagonal structure and $|\Psi_6| < 1$ when it deviates from the hexagonal symmetry. The orientation θ changes by approximately 12° and, on average, the hexagonality is

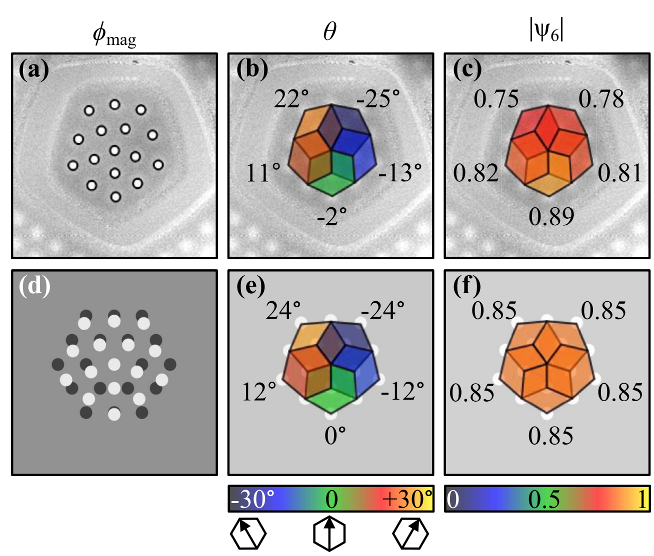

FIG. 5. Structural analysis and linear elastic theory. (a) Positions of the skyrmions in the magnetic phase image. (b) Orientation θ and (c) hexagonality $|\Psi_6|$ maps calculated from the positions in (a). (d) Fivefold disclination model calculated using linear elastic theory. (e) Corresponding orientation and (f) hexagonality maps.

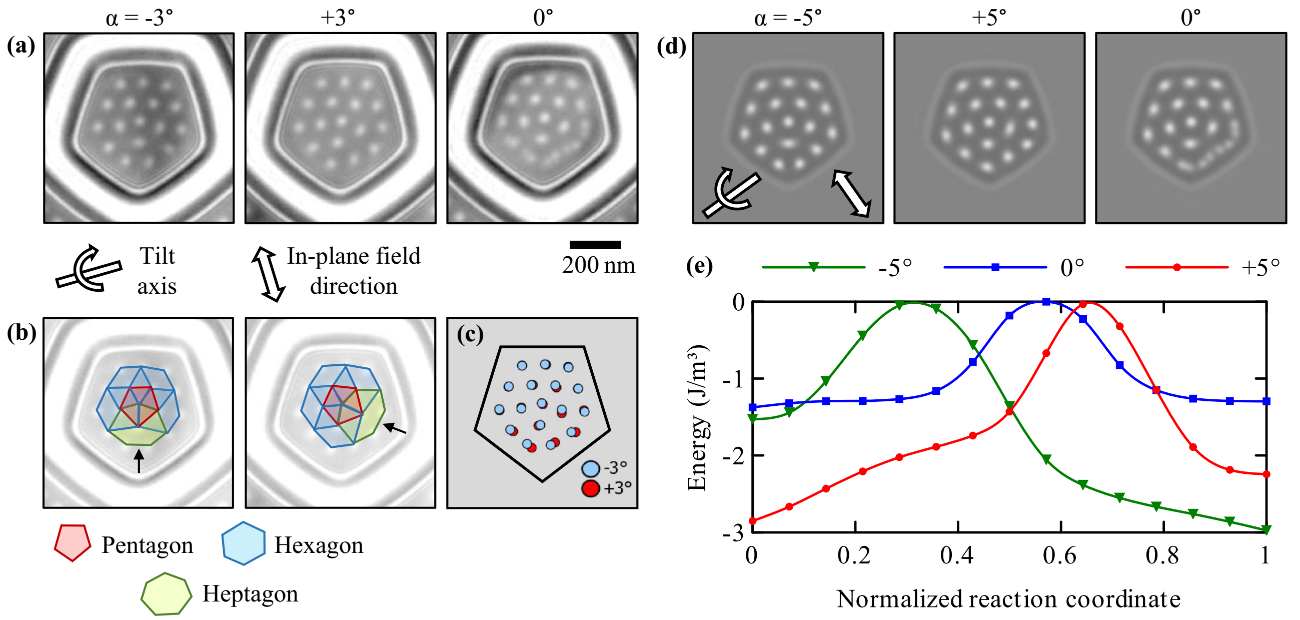

FIG. 6. Skyrmion mobility around a disclination. (a) Fresnel images of a skyrmion lattice with $S = 17$ obtained in the presence of an external magnetic field of 230 mT at different tilt angles $\alpha = -3^\circ, +3^\circ$, and 0°. (b) Images obtained at -3° and $+3^\circ$ overlaid with pentagons, hexagons, and heptagons. (c) Positions of the skyrmions in the two tilted images represented by blue and red dots. (d) Lorentz images calculated from micromagnetic simulations showing the lowest-energy configuration at $\alpha = -5^\circ$ and $+5^\circ$ tilt angles. The image at 0° is the sum of the previous images. (e) Energy paths for the transition between the two lattice configurations calculated for the three different tilt angles $\pm 5^\circ$ and 0°.

$\langle|\Psi_6|\rangle = 0.81$. For comparison, a disclination model was calculated using linear elastic theory. We assumed that the skyrmion lattice can be described as elastically isotropic with a Poisson's ratio $\nu = \frac{1}{3}$ [43]. In isotropic linear elastic theory, the displacement produced by a disclination is given in polar coordinates (r, θ) by

$$u_r = \frac{\Omega}{4\pi} r \left[\frac{1-2\nu}{1-\nu} \ln\left(\frac{r}{R}\right) - 1\right], \quad u_\theta = \frac{\Omega}{2\pi}\theta r, \tag{3}$$

with Ω the characteristic rotation angle of the disclination ($\Omega = \frac{\pi}{3}$ in the case of a fivefold disclination) and R the size of the system [44]. The white dots in Fig. 5(d) show the fivefold disclination created from a hexagonal lattice (black dots) using Eq. (3). Figures 5(e) and 5(f) show the corresponding orientation and hexagonality maps calculated from the positions in Fig. 5(d). The orientation changes by $\Delta\theta = 12^\circ$ and the hexagonality is $|\Psi_6| = 0.85$, which is close to the average experimental values. A similar treatment of a sevenfold disclination is also shown in the Supplemental Material 5 [39].

D. Mobility of skyrmions around a disclination

It was observed in Fig. 3 that when $S = 17$ skyrmions, a 5–7 dislocation is created in the lattice. The 7-coordinated skyrmion can be located in any of the five corners of the pentagon, leading to five geometrically equivalent configurations. Switching between the five configurations can be done by adding an in-plane component to the magnetic field, which can be produced by tilting the sample with respect to the electron beam. Figure 6(a) shows Fresnel images acquired at different tilt angles $\alpha = -3^\circ, +3^\circ$, and 0°. At -3°, the 7-coordinated skyrmion of the dislocation is located in the bottom corner of the pentagon, as shown schematically in Fig. 6(b). At $+3^\circ$, it is located in the bottom-right corner. Interestingly, at an intermediate angle of 0°, the skyrmions along the bottom-right edge wobble between the two states, leading to a diffuse appearance. In Fig. 6(c), the positions of the skyrmions measured at $+3^\circ$ and -3° are indicated by blue and red circles to show their relative displacements. Between the two tilted states, the skyrmions near the bottom-right edge are displaced along the circular direction, which explains their diffuse appearance at 0°. Another interesting case of wobbling in a larger pentagon with three rings is described in the Supplemental Material 7 [39].

To understand this phenomenon, we performed micromagnetic simulations. The external field was applied with a tilt of 5° with respect to the normal, and the in-plane component is oriented perpendicular to one of the pentagon sides, closely matching the experimental conditions. Figure 6(d) shows the simulated Lorentz images of the lowest-energy states at -5° and $+5^\circ$. The 0° image was obtained by averaging the two previous configurations. The minimum-energy paths shown in Fig. 6(e) illustrate that at 0° tilt, the two configurations are almost degenerate, whereas at $\pm 5^\circ$, one state becomes significantly lower in energy than the other, depending on the sign of the tilt angle. Furthermore, the energy barrier separating the states increases strongly under tilt, compared to the zero-tilt case. This explains why sequential switching between states, leading to diffuse contrast, occurs only at zero tilt, where the barrier is minimal.

III. DISCUSSION

Pentagons and heptagon-shaped geometries have been created by focused ion beam in order to stabilize fivefold and sevenfold disclinations. The disclination state corresponds to a specific number of skyrmions which depends on the size of the sample and the number of skyrmion rings it can contain. At 220 K, the number of skyrmions varies stochastically during field cycling, and depending on the skyrmion number, their spatial distribution can be influenced by slight geometric irregularities. Experimentally, we found that the probability to obtain the disclination state when performing multiple cycles is 12% for $N = 2$ skyrmion rings. We were also able to obtain disclinations with $N = 3$ skyrmion rings (see the Supplemental Material 6 [39]), but the probability is particularly low for this size.

Structural analysis of the fivefold and sevenfold disclinations shows, respectively, an increase and a decrease of the interskyrmion distance along the circular direction, due to the removal or the addition of a wedge. Orientational and hexagonality maps derived from experimental images were found to be in agreement with those calculated from linear elastic theory. The shape of the skyrmions at low field is also modified by the disclination strain. In the fivefold case, the central skyrmion shows a pentagonal shape and is smaller than the surrounding skyrmions due to the compressive strain towards the center of the disclination. The surrounding skyrmions show an elliptical deformation along the circular direction around the core, which depends strongly on the applied magnetic field and can be associated with a twist along the thickness of the sample according to simulations. In the case of a sevenfold disclination, the central skyrmion is slightly larger due to the tensile strain and there is an elongation of the surrounding skyrmions along the radial direction.

Finally, the mobility of skyrmions around a disclination was investigated. When the rotation symmetry of the outer skyrmion ring is broken due to the presence of dislocations, the lattice can exhibit multiple metastable configurations where the dislocations shift to different corners of the geometry. Overcoming the energy barrier and switching between the different configurations can be done by tilting the sample a few degrees with respect to the out-of-plane field in order to introduce a small in-plane component. At the temperature of the experiment (220 K), and when an intermediate angle is reached, the thermal energy allows the system to overcome the small barrier between two states. The skyrmion lattice can then wobble between two configurations, leading to a smeared appearance of the skyrmions in the images. This phenomenon is expected to vanish at low temperature as the system should remain trapped in a local minimum.

IV. CONCLUSION

Single-crystal FeGe nanostructures with pentagonal and heptagonal shapes were fabricated by focused ion beam. This allowed us to stabilize fivefold and sevenfold disclinations in the skyrmion lattice solid phase with relatively low external magnetic fields. The disclinated lattices observed using Lorentz TEM and off-axis electron holography were in agreement with micromagnetic simulations and their structure agreed with linear elastic theory. It was also shown that skyrmion rings around a disclination can switch between energetically equivalent configurations when dislocations are present. These results demonstrate that geometric confinement is an effective strategy for engineering defects in skyrmion lattices of chiral magnets. Future work could explore the controlled creation and annihilation of individual disclinations using different stimuli such as light, current pulses, or mechanical strain.

ACKNOWLEDGMENTS

This work was supported by the European Union's Horizon 2020 Research and Innovation Programme under Grant Agreement No. 856538 (project "3D MAGIC"). V.M.K. acknowledges the financial support from the European Union's Horizon Europe Research and Innovation Programme under the Marie Skłodowska-Curie Grant Agreement No. 101203692 (QUANTHOPF).

T.D. conceived the study, performed the LTEM experiments, and wrote the manuscript. N.S.K. performed micromagnetic simulations. V.M.K. performed calculations of energy paths. R.E.D.-B. secured funding for the study.

The authors declare no competing interests.

DATA AVAILABILITY

The data that support the findings of this article are publicly available [45].

APPENDIX A: SAMPLE PREPARATION AND LORENTZ TEM

TEM lamellae were prepared from a bulk crystal of FeGe using 30 kV focused Ga^+ ion beam sputtering in a Thermo Fisher Scientific (TFS) scanning electron microscope (FIB-SEM) Helios dual-beam platform. The samples were patterned following the protocol described in the Supplemental Material 1 [39]. The final thickness of the lamellae was in the 100 to 150 nm range.

TEM was carried out using two TFS Titan microscopes named Titan T [46] and Titan Holo [47], both equipped with a Schottky field emission gun operated at 300 kV, a CEOS image aberration corrector, a postspecimen electron biprism, and a field-free Lorentz mode. Titan T is equipped with a $2\,\mathrm{k} \times 2\,\mathrm{k}$ Gatan CCD Ultrascan 1000P and Titan Holo is equipped with a $4\,\mathrm{k} \times 4\,\mathrm{k}$ Gatan K2-IS direct electron detector. The objective lens was used to apply magnetic fields perpendicular to the sample which were precalibrated using a Hall probe. The temperature of the sample was controlled using a Gatan liquid-nitrogen-cooled specimen holder (model 636) and temperature controller (model 1905).

When electrons pass through a magnetic induction field $B_\perp$ that is oriented perpendicular to their trajectory, they are deflected by the Lorentz force. To a first approximation, the deflection angle is given by the expression $\theta = \frac{e\lambda}{h} B_\perp t$, where e is the electron charge, λ is the electron wavelength, t is the specimen thickness, and h is Planck's constant [48]. When Fresnel images are recorded in a defocused plane, the deflection of the electron beam leads to contrast variations at the position of magnetic domain walls, whose width and amplitude depend on the defocus.

In this manuscript, the images were recorded at a temperature of 220 K with a defocus of 500 μm.

APPENDIX B: OFF-AXIS ELECTRON HOLOGRAPHY

In off-axis electron holography, a postspecimen electron biprism is used to overlap a wave traveling through the sample (object wave) with a wave traveling in vacuum (reference wave). The condenser stigmators are used to form an elliptical illumination to improve the coherence in the direction perpendicular to the biprism. We consider a reference wave $\psi_1 = A_1 \exp(i\phi_1)$ traveling in a uniform region (vacuum for instance) and an object wave $\psi_2 = A_2(\vec{r})\exp[i\phi_2(\vec{r})]$ passing through a sample, where $A_1, A_2(\vec{r})$ and $\phi_1, \phi_2(\vec{r})$ are their respective amplitudes and phases. The intensity distribution of an off-axis electron hologram can be expressed as

$$I_{\text{holo}}(\vec{r}) = A_1^2 + A_2^2(\vec{r}) + I_{\text{inel}}(\vec{r}) + 2\mu A_1 A_2(\vec{r})\cos[\Delta\phi(\vec{r}) + 2\pi\vec{q}_c.\vec{r}], \tag{B1}$$

where $I_{\text{inel}}(\vec{r})$ is the inelastic background, μ is the fringe contrast, $\Delta\phi(\vec{r}) = \phi_1 - \phi_2(\vec{r})$ is the phase change of the object wave with respect to the reference wave, and $\vec{q}_c$ is the carrier frequency [49]. The Fourier transform of the hologram can be described as

$$\begin{aligned} \text{FT}\{I_{\text{holo}}(\vec{r})\} = \text{FT}\big\{A_1^2 + A_2^2(\vec{r}) + I_{\text{inel}}(\vec{r})\big\} \quad & \text{centerband} \\ + \mu\text{FT}\{A_1A_2(\vec{r})\exp[i\Delta\phi(\vec{r})]\} \otimes \delta(\vec{q} + \vec{q}_c) \quad & \text{sideband 1} \\ + \mu\text{FT}\{A_1A_2(\vec{r})\exp[i\Delta\phi(\vec{r})]\} \otimes \delta(\vec{q} - \vec{q}_c) \quad & \text{sideband 2.} \end{aligned} \tag{B2}$$

An aperture is applied to a sideband, which is then shifted to the center of Fourier space. Using an inverse Fourier transform, the following images are reconstructed:

$$\begin{aligned} C_{\text{rec}}(\vec{r}) &= \mu A_1 A_2(\vec{r})\exp(i\Delta\phi(\vec{r})), \\ A_{\text{rec}}(\vec{r}) &= \mu A_1 A_2(\vec{r}) = \sqrt{\text{Re}^2 + \text{Im}^2}, \\ \phi_{\text{rec}}(\vec{r}) &= \Delta\phi(\vec{r}) = \arctan(\text{Im}/\text{Re}), \end{aligned} \tag{B3}$$

where $C_{\text{rec}}(\vec{r})$ is a complex image, and $A_{\text{rec}}(\vec{r})$ and $\phi_{\text{rec}}(\vec{r})$ are the corresponding amplitude and phase images.

The phase change $\Delta\phi$ has an electrostatic $\Delta\phi_{\text{elec}}$ and a magnetic $\Delta\phi_{\text{mag}}$ component according to the expressions (in one dimension) [50]

$$\begin{aligned} \Delta\phi(x) &= \Delta\phi_{\text{elec}} + \Delta\phi_{\text{mag}}, \\ \Delta\phi(x) &= C_E \int V_0(x,z)dz - \frac{e}{\hbar}\iint B_\perp(x,z)dxdz, \end{aligned} \tag{B4}$$

where z is the direction of the incident electron beam, x is a direction perpendicular to z, C_E is an interaction constant that depends on the electron energy, V_0 is the mean inner potential (MIP) of the specimen, $B_\perp$ is the component of the magnetic induction field that is perpendicular to both x and z, e is the electron charge, and $\hbar$ is the reduced Planck's constant. Here, the phase variations related to the thickness and the electrostatic component have been removed by subtracting a phase image recorded above the Curie temperature to the phase image obtained at low temperature. The magnetic phase term can then be simplified to

$$\Delta\phi_{\text{mag}}(x) = -\frac{et}{\hbar}\int B_\perp(x)dx, \tag{B5}$$

where t is the specimen thickness. The derivative of the magnetic phase is proportional to the magnetic induction field according to the expression

$$\frac{d[\Delta\phi_{\text{mag}}(x)]}{dx} = -\frac{e}{\hbar}B_\perp(x). \tag{B6}$$

Phase images and color-coded magnetic induction maps were reconstructed using the DIGITAL MICROGRAPH software (Gatan) and the HOLOWORKS plugin [51].

To map the local orientation parameter, the subpixel coordinates of the skyrmions' center of mass in the electron phase image were determined after applying a Gaussian filter to the image. Nearest neighbors were then determined manually and the angles θ_{jk} were calculated from the coordinates of the skyrmions using $a$tan2 functions. The complex value of Ψ_6, the orientation $\theta = \arg(\Psi_6)/6$, and the hexagonality $|\Psi_6|$ were then calculated for each skyrmion.

APPENDIX C: MICROMAGNETIC SIMULATIONS

We employ the standard micromagnetic model for isotropic chiral magnets, which includes four energy contributions: the Heisenberg exchange, the Dzyaloshinskii-Moriya interaction (DMI), the Zeeman energy from the external magnetic field, and the energy of demagnetizing fields arising from the sample itself. The corresponding energy functional can be written as follows [52]:

$$\begin{aligned} \mathcal{E} = \int_{V_{\text{m}}} d\mathbf{r}\bigg[\mathcal{A}\sum_{i=x,y,z}|\nabla m_i|^2 + \mathcal{D}\mathbf{m}\cdot(\nabla\times\mathbf{m}) \\ - M_{\text{s}}\mathbf{m}\cdot(\mathbf{B}_{\text{ext}} + \nabla\times\mathbf{A}_{\text{d}})\bigg] + \frac{1}{2\mu_0}\int_{\mathbb{R}^3} d\mathbf{r}\sum_{i=x,y,z}|\nabla A_{\text{d},i}|^2, \end{aligned} \tag{C1}$$

where V_{m} is the volume of the magnetic sample, $\mathbf{m}(\mathbf{r}) = \mathbf{M}(\mathbf{r})/M_{\text{s}}$ denotes the magnetization vector field, M_{s} is the saturation magnetization, μ_0 is the vacuum permeability, and $\mathcal{A}$ and $\mathcal{D}$ are the Heisenberg exchange constant and DMI constant, respectively. $\mathbf{A}_{\text{d}}(\mathbf{r})$ is the magnetic vector potential induced by the sample magnetization and $\mathbf{B}_{\text{ext}}$ is the external magnetic field.

We assume the material parameter for FeGe [41,52–54]: $\mathcal{A} = 4.75$ pJ/m, $\mathcal{D} = 0.853$ mJ/m^2, $\mathbf{M}_{\text{s}} = 384$ kA/m. The above parameters are optimized for the temperature of 95 K. The experiments presented in this work are performed at the elevated temperature of 220 K. To account for this aspect, we use a reduced value of the saturation magnetization, $M_s = 120$ kA/m, which yields quantitative agreement with experimental observations, as shown in Fig. 4 and in the Supplemental Material, Fig. S4 [39]. Simulations were performed on a regular mesh of $256 \times 256 \times 64$ cuboids. The cuboid dimensions were chosen to reproduce the geometry of the experimental samples. Specifically, for the pentagon, we set the cuboid size to $2.014 \times 2.014 \times 2.12$ nm^3, while for the heptagon-shaped sample shown in the Supplemental Material, Figs. S3e and S4f–S4j, we used $2.15 \times 2.15 \times 2.12$ nm^3 [39]. To account for uncertainty in the exact sample size, we varied the simulated dimensions within a range of $\pm 10\%$. For the pentagon [Figs. 3(c), 4(f)–4(j), and 6(d)], the best agreement was obtained for a simulated sample 5% smaller than the measured size, whereas for the heptagon, the best fit corresponded to the experimentally determined size.

We simulate the FIB-damaged layer by setting $\mathcal{D}$ to zero in a thin layer of cuboids on all edges of the sample [55]. We find the best agreement between experimental and theoretical images for the thickness of the FIB-damaged layer of 24 nm. This corresponds to a layer of approximately 12 cuboids from each side of the sample. Additional micromagnetic simulations with varying thickness of the damaged layers are discussed in the Supplemental Material 8 [39]. For better agreement with the experiment, we modified the sharp linear edges of the pentagon and heptagon to slightly curved ones. More precisely, the sides of the pentagon are approximated by arcs of a circle passing through adjacent vertices of the polyhedron. The radius of this circle is three times larger than the radius of the circumscribed circle of the regular polyhedron. In the case of a pentagon and a heptagon, the centers of the circles are positioned on opposite sides with respect to the polyhedron's side, exhibiting positive and negative curvature, respectively. The micromagnetic simulations were performed using the EXCALIBUR [56] code, which enables efficient energy minimization and *in situ* calculation of Lorentz TEM images according to the method described in the following Appendix. Additionally, we verified our results using the open-source software MUMAX [57].

APPENDIX D: SIMULATION OF MAGNETIC PHASE AND FRESNEL IMAGES

Using the phase object approximation, the wave function of an electron beam can be written as follows [58]:

$$\Psi_0(x, y) \propto \exp[i\phi_{\text{mag}}(x, y)], \tag{D1}$$

where $\phi_{\text{mag}}(x, y)$ is the magnetic contribution to the phase shift [49]

$$\phi_{\text{mag}}(x, y) = -\frac{e}{\hbar}\int_{-\infty}^{+\infty} A_z dz, \tag{D2}$$

with e an elementary charge and $\hbar$ the reduced Planck's constant. The z component A_z of the magnetic vector potential was obtained from micromagnetic simulations. Neglecting aberrations other than defocus, the wave function at the detector plane can be written in the form

$$\Psi_{\Delta z}(x, y) \propto \iint \Psi_0(x', y')K(x - x', y - y')dx'dy', \tag{D3}$$

where the kernel is given by the expression

$$K(\xi, \eta) = \exp\left[\frac{i\pi}{\lambda\Delta z}(\xi^2 + \eta^2)\right], \tag{D4}$$

where λ is the electron wavelength and Δz is the defocus. The Fresnel image intensity is then calculated following

$$I(x, y) \propto |\Psi_{\Delta z}(x, y)|^2.$$

For more details, see Ref. [41].

APPENDIX E: MINIMUM-ENERGY PATH CALCULATION

To study the transition mechanism between two states corresponding to different packings of 17 skyrmions in the pentagon-shaped sample, we calculated the minimum energy path (MEP) between these configurations using the geodesic nudged elastic band (GNEB) method [59,60]. The GNEB method yields a sequence of transient states that form a discrete MEP. These transient states, representing snapshots of the system along the transition, are referred to as images. The number of images is a free parameter, chosen to balance the continuity of the energy path with computational efficiency. The method is iterative, starting from an initial guess for the path that is usually constructed by linear interpolation between the initial and final spin configurations. At each iteration, we applied the velocity projection optimization algorithm. According to the GNEB method, all neighboring images must remain equidistant in the geodesic spin space. This constraint is enforced by effective forces, which combine the spin effective fields with an additional spring force proportional to the Euclidean distance between images. Besides the transient states, the GNEB method also identifies the saddle-point configuration along the MEP. From the saddle-point energy, one can estimate the energy barrier that must be overcome for the transition between states. Assuming that the height of the energy barrier is comparable to $k_B T$, the GNEB results can be directly compared with finite-temperature simulations of the stochastic LLG equation [61]. We implemented the GNEB method in our extension [62,63] of the MUMAX software [57] and used it for the MEP calculations shown in Fig. 6(e). For consistency with the micromagnetic simulations, we used the same material parameters: $\mathcal{A} = 4.75$ pJ/m, $\mathcal{D} = 0.853$ mJ/m^2, and $M_{\text{sat}} = 120$ kA/m. The shape and size of the simulated domain are identical to those in micromagnetic simulations performed with EXCALIBUR: the mesh density is set to $256 \times 256 \times 64$ cuboids and each cuboid size is $2.014 \times 2.014 \times 2.12$ nm^3. We further assumed a FIB-damaged layer of thickness 24 nm around all sample edges, approximated by setting $\mathcal{D} = 0$ in the corresponding cuboids. For details, see the script provided in the Supplemental Material 9 [39] and initial states are available at Ref. [64]. Note that this script is compatible only with the extended version of MUMAX [62].

[1] F. H. C. Crick and J. D. Watson, Structure of small viruses, Nature (London) **177**, 473 (1956).

[2] J. Walz, T. Tamura, N. Tamura, R. Grimm, W. Baumeister, and A. J. Koster, Tricorn protease exists as an icosahedral supermolecule in vivo, Mol. Cell **1**, 59 (1997).

[3] G. Rose, Ueber die krystallformen des goldes und des silbers, Ann. Phys. **99**, 196 (1831).

[4] A. Von Lasaulx, On twin crystals of native copper from the Ohligerzug mine near Daaden, Proc. Lower Rhenish Soc. Nat. Med. Sci. Bonn **39**, 95 (1882).

[5] J. G. Allpress and J. V. Sanders, The structure and orientation of crystals in deposits of metals on mica, Surf. Sci. **7**, 1 (1967).

[6] S. Ino, Stability of multiply-twinned particles, J. Phys. Soc. Jpn. **27**, 941 (1969).

[7] H. Hofmeister, Forty years study of fivefold twinned structures in small particles and thin films, Cryst. Res. Technol. **33**, 3 (1998).

[8] V. Volterra, Sur l'équilibre des corps élastiques multiplement connexes, Ann. Sci. Ec. Norm. Super. **24**, 401 (1907).

[9] R. deWit, Theory of disclinations: IV. Straight disclinations, J. Res. Natl. Bur. Stand. **77A**, 607 (1973).

[10] F. C. Frank, I. Liquid crystals. On the theory of liquid crystals, Discuss. Faraday Soc. **25**, 19 (1958).

[11] D. Shechtman, I. Blech, D. Gratias, and J. W. Cahn, Metallic phase with long-range orientational order and no translational symmetry, Phys. Rev. Lett. **53**, 1951 (1984).

[12] C. L. Johnson, E. Snoeck, M. Ezcurdia, B. Rodríguez-González, I. Pastoriza-Santos, L. M. Liz-Marzán, and M. J. Hÿtch, Effects of elastic anisotropy on strain distributions in decahedral gold nanoparticles, Nat. Mater. **7**, 120 (2008).

[13] M. J. Walsh, K. Yoshida, A. Kuwabara, M. L. Pay, P. L. Gai, and E. D. Boyes, On the structural origin of the catalytic properties of inherently strained ultrasmall decahedral gold nanoparticles, Nano Lett. **12**, 2027 (2012).

[14] A. A. Golovin and A. A. Nepomnyashchy, Disclinations in square and hexagonal patterns, Phys. Rev. E **67**, 056202 (2003).

[15] Y. Ishida and S. Iyama, Observation of wedge disclinations and their behavior in a bubble raft crystal, Acta Metall. **24**, 417 (1976).

[16] Y. Liu, S. Leung, F.-F. Li, Z.-K. Lin, X. Tao, Y. Poo, and J.-H. Jiang, Bulk-disclination correspondence in topological crystalline insulators, Nature (London) **589**, 381 (2021).

[17] O. V. Yazyev and S. G. Louie, Topological defects in graphene: Dislocations and grain boundaries, Phys. Rev. B **81**, 195420 (2010).

[18] J.-C. Charlier, Defects in carbon nanotubes, Acc. Chem. Res. **35**, 1063 (2002).

[19] M. J. Bowick and L. Giomi, Two-dimensional matter: Order, curvature and defects, Adv. Phys. **58**, 449 (2009).

[20] A. Fert, N. Reyren, and V. Cros, Magnetic skyrmions: Advances in physics and potential applications, Nat. Rev. Mater. **2**, 17031 (2017).

[21] S. Muülbauer, B. Binz, F. Jonietz, C. Pfleiderer, A. Rosch, A. Neubauer, R. Georgii, and P. Böni, Skyrmion lattice in a chiral magnet, Science **323**, 915 (2009).

[22] X. Z. Yu, Y. Onose, N. Kanazawa, J. H. Park, J. H. Han, Y. Matsui, N. Nagaosa, and Y. Tokura, Real-space observation of a two-dimensional skyrmion crystal, Nature (London) **465**, 901 (2010).

[23] I. Dzyaloshinsky, A thermodynamic theory of "weak" ferromagnetism of antiferromagnetics, J. Phys. Chem. Solids **4**, 241 (1958).

[24] T. Moriya, Anisotropic superexchange interaction and weak ferromagnetism, Phys. Rev. **120**, 91 (1960).

[25] X. Z. Yu, N. Kanazawa, Y. Onose, K. Kimoto, W. Z. Zhang, S. Ishiwata, Y. Matsui, and Y. Tokura, Near room-temperature formation of a skyrmion crystal in thin-films of the helimagnet FeGe, Nat. Mater. **10**, 106 (2011).

[26] Z.-A. Li, F. Zheng, A. H. Tavabi, J. Caron, C. Jin, H. Du, A. Kovács, M. Tian, M. Farle, and R. E. Dunin-Borkowski, Magnetic skyrmion formation at lattice defects and grain boundaries studied by quantitative off-axis electron holography, Nano Lett. **17**, 1395 (2017).

[27] S. Pöllath, J. Wild, L. Heinen, T. N. G. Meier, M. Kronseder, L. Tutsch, A. Bauer, H. Berger, C. Pfleiderer, J. Zweck, A. Rosch, and C. H. Back, Dynamical defects in rotating magnetic skyrmion lattices, Phys. Rev. Lett. **118**, 207205 (2017).

[28] T. Schönenberger, P. Huang, L. D. Brun, L. Guanghao, A. Magrez, F. Carbone, and H. M. Rønnow, Direct visualisation of skyrmion lattice defect alignment at grain boundaries, Nanoscale Res. Lett. **17**, 20 (2022).

[29] J. Rajeswari, P. Huang, G. F. Mancini, Y. Murooka, T. Latychevskaia, D. McGrouther, M. Cantoni, E. Baldini, J. S. White, A. Magrez, T. Giamarchi, H. M. Rønnow, and F. Carbone, Filming the formation and fluctuation of skyrmion domains by cryo-Lorentz transmission electron microscopy, Proc. Natl. Acad. Sci. **112**, 14212 (2015).

[30] P. Huang, T. Schönenberger, M. Cantoni, L. Heinen, A. Magrez, A. Rosch, F. Carbone, and H. M. Rønnow, Melting of a skyrmion lattice to a skyrmion liquid via a hexatic phase, Nat. Nanotechnol. **15**, 761 (2020).

[31] J. Zázvorka, F. Dittrich, Y. Ge, N. Kerber, K. Raab, T. Winkler, K. Litzius, M. Veis, P. Virnau, and M. Kläui, Skyrmion lattice phases in thin film multilayer, Adv. Funct. Mater. **30**, 2004037 (2020).

[32] A. R. C. McCray, Y. Li, R. Basnet, K. Pandey, J. Hu, D. P. Phelan, X. Ma, A. K. Petford-Long, and C. Phatak, Thermal hysteresis and ordering behavior of magnetic skyrmion lattices, Nano Lett. **22**, 7804 (2022).

[33] P. Meisenheimer, H. Zhang, D. Raftrey, X. Chen, Y.-T. Shao, Y.-T. Chan, R. Yalisove, R. Chen, J. Yao, M. C. Scott, W. Wu, D. A. Muller, P. Fischer, R. J. Birgeneau, and R. Ramesh, Ordering of room-temperature magnetic skyrmions in a polar van der Waals magnet, Nat. Commun. **14**, 3744 (2023).

[34] J. M. Kosterlitz and D. J. Thouless, Ordering, metastability and phase transitions in two-dimensional systems, J. Phys. C **6**, 1181 (1973).

[35] B. I. Halperin and D. R. Nelson, Theory of two-dimensional melting, Phys. Rev. Lett. **41**, 121 (1978).

[36] A. P. Young, Melting and the vector Coulomb gas in two dimensions, Phys. Rev. B **19**, 1855 (1979).

[37] A. Dussaux, P. Schoenherr, K. Koumpouras, J. Chico, K. Chang, L. Lorenzelli, N. Kanazawa, Y. Tokura, M. Garst, A. Bergman, C. L. Degen, and D. Meier, Local dynamics of topological magnetic defects in the itinerant helimagnet FeGe, Nat. Commun. **7**, 12430 (2016).

[38] P. Schoenherr, J. Müller, L. Köhler, A. Rosch, N. Kanazawa, Y. Tokura, M. Garst, and D. Meier, Topological domain walls in helimagnets, Nat. Phys. **14**, 465 (2018).

[39] See Supplemental Material at http://link.aps.org/supplemental/10.1103/nwd2-1hk9 for details of sample preparation, additional LTEM field series, analysis of sevenfold disclinations, magnetic field evolution, disclinations in samples of different sizes, skyrmion mobility, influence of the FIB-damaged layer, and GNEB simulation scripts.

[40] T. Denneulin, A. Kovács, R. Boltje, N. S. Kiselev, and R. E. Dunin-Borkowski, Geometric phase analysis of magnetic skyrmion lattices in Lorentz transmission electron microscopy images, Sci. Rep. **14**, 12286 (2024).

[41] F. Zheng, F. N. Rybakov, N. S. Kiselev, D. Song, A. Kovács, H. Du, S. Blügel, and R. E. Dunin-Borkowski, Magnetic skyrmion braids, Nat. Commun. **12**, 5316 (2021).

[42] D. R. Nelson and B. I. Halperin, Dislocation-mediated melting in two dimensions, Phys. Rev. B **19**, 2457 (1979).

[43] S. P. Kang, H. Y. Kwon, and C. Won, Elastic moduli and Poisson's ratio of 2-dimensional magnetic skyrmion lattice, J. Appl. Phys. **121**, 203902 (2017).

[44] R. d. Wit, Partial disclinations, J. Phys. C **5**, 529 (1972).

[45] T. Denneulin *et al.*, Magnetic skyrmion lattice disclinations in pentagon- and heptagon-shaped FeGe nanostructures, Zenodo, 2026, https://doi.org/10.5281/zenodo.18111798.

[46] A. Thust, J. Barthel, and K. Tillmann, FEI Titan 80-300 TEM, J. Large-scale Res. Facil. (JLSRF) **2**, A41 (2016).

[47] C. Boothroyd, A. Kovács, and K. Tillmann, FEI Titan G2 60-300 HOLO, J. Large-scale Res. Facil. (JLSRF) **2**, A44 (2016).

[48] J. N. Chapman, The investigation of magnetic domain structures in thin foils by electron microscopy, J. Phys. D: Appl. Phys. **17**, 623 (1984).

[49] H. Lichte and M. Lehmann, Electron holography - basics and applications, Rep. Prog. Phys. **71**, 016102 (2008).

[50] M. R. McCartney and D. J. Smith, Electron holography: Phase imaging with nanometer resolution, Annu. Rev. Mater. Res. **37**, 729 (2007).

[51] E. Völkl, L. F. Allard, and B. Frost, A software package for the processing and reconstruction of electron holograms, J. Microsc. **180**, 39 (1995).

[52] F. Zheng, N. S. Kiselev, F. N. Rybakov, L. Yang, W. Shi, S. Blügel, and R. E. Dunin-Borkowski, Hopfion rings in a cubic chiral magnet, Nature (London) **623**, 718 (2023).

[53] F. Zheng, F. N. Rybakov, A. B. Borisov, D. Song, S. Wang, Z.-A. Li, H. Du, N. S. Kiselev, J. Caron, A. Kovács, M. Tian, Y. Zhang, S. Blügel, and R. E. Dunin-Borkowski, Experimental observation of chiral magnetic bobbers in B20-type FeGe, Nat. Nanotechnol. **13**, 451 (2018).

[54] F. Zheng, N. S. Kiselev, L. Yang, V. M. Kuchkin, F. N. Rybakov, S. Blügel, and R. E. Dunin-Borkowski, Skyrmion–antiskyrmion pair creation and annihilation in a cubic chiral magnet, Nat. Phys. **18**, 863 (2022).

[55] A. S. Savchenko, F. Zheng, N. S. Kiselev, L. Yang, F. N. Rybakov, S. Blügel, and R. E. Dunin-Borkowski, Diversity of states in a chiral magnet nanocylinder, APL Mater. **10**, 061110 (2022).

[56] F. N. Rybakov and E. Babaev, Quantum and classical solutions international AB, EXCALIBUR software, http://quantumandclassical.com/excalibur/.

[57] A. Vansteenkiste, J. Leliaert, M. Dvornik, M. Helsen, F. Garcia-Sanchez, and B. Van Waeyenberge, The design and verification of MuMax3, AIP Adv. **4**, 107133 (2014).

[58] M. De Graef, 2. Lorentz microscopy: Theoretical basis and image simulations, in *Magnetic Imaging and Its Applications to Materials* (Elsevier, Amsterdam, 2001), pp. 27–67.

[59] P. F. Bessarab, V. M. Uzdin, and H. Jónsson, Method for finding mechanism and activation energy of magnetic transitions, applied to skyrmion and antivortex annihilation, Comput. Phys. Commun. **196**, 335 (2015).

[60] P. F. Bessarab, Comment on "Path to collapse for an isolated Néel skyrmion", Phys. Rev. B **95**, 136401 (2017).

[61] V. M. Kuchkin, P. F. Bessarab, and N. S. Kiselev, Thermal generation of droplet soliton in chiral magnet, Phys. Rev. B **105**, 184403 (2022).

[62] V. M. Kuchkin, Regularized LLG simulations MuMax3 (extension), Github repository, 2023, https://github.com/kuchkin/mumax3-gneb.

[63] V. M. Kuchkin, U. B. Arnalds, H. Jónsson, and P. F. Bessarab, Coexisting mechanisms of thermally driven magnetization reversal in Shakti spin ice systems, Phys. Rev. Res. **7**, 033209 (2025).

[64] V. Kuchkin *et al.*, Initial states for GNEB method simulations [Data set], Zenodo, 2025, https://doi.org/10.5281/zenodo.17234039.